

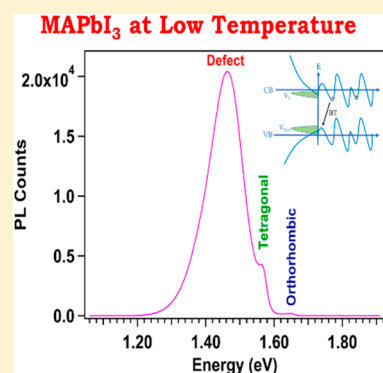
# Charge Compensating Defects in Methylammonium Lead Iodide Perovskite Suppressed by Formamidinium Inclusion

Niraj Shrestha,<sup>#</sup> Zhaoning Song,<sup>#</sup> Cong Chen, Ebin Bastola,<sup>ib</sup> Xiaoming Wang,<sup>ib</sup> Yanfa Yan,<sup>ib</sup> and Randy J. Ellingson<sup>\*ib</sup>

Department of Physics and Astronomy, Wright Center for Photovoltaics Innovation and Commercialization, University of Toledo, Toledo, Ohio 43606, United States

## Supporting Information

**ABSTRACT:** Temperature-dependent photoluminescence (PL) spectroscopy measurements have been performed over a range from 9 K to room temperature on polycrystalline methylammonium (MA)/formamidinium (FA) lead iodide ( $\text{MA}_{1-x}\text{FA}_x\text{PbI}_3$ ) perovskite thin films. Our low-temperature PL analysis reveals the existence of charge compensating defects in  $\text{MAPbI}_3$ , which may explain the lower net free carrier concentration in  $\text{MAPbI}_3$  perovskite. More interestingly, we observe the suppression of the PL emission associated with the charged defects by appropriate FA inclusion. Furthermore, FA incorporation into  $\text{MAPbI}_3$  has been found to slow the phase transformation of  $\text{MA}_{1-x}\text{FA}_x\text{PbI}_3$  from orthorhombic to tetragonal phase, which occurs with increasing temperature. Our analyses of the FA concentration's impact on defect density and structural phase transformation provide beneficial insights that improve the understanding of the photovoltaic properties and application of organic–inorganic metal halide perovskites.



Organic–inorganic metal halide perovskite materials offer great promise in photovoltaic (PV) applications due to their direct band gaps with large absorption coefficients,<sup>1,2</sup> long electron–hole diffusion lengths,<sup>1,3</sup> low exciton binding energies,<sup>4</sup> low-temperature solution processability,<sup>5</sup> and low fabrication costs.<sup>6</sup> Although small-sized solar cells based on metal halide perovskites have already reached a certified power conversion efficiency of 25.2%,<sup>7</sup> intrinsic and extrinsic material instability issues,<sup>8–11</sup> along with other commercialization challenges such as large-scale manufacturing,<sup>12</sup> unstabilized power output,<sup>13</sup> and toxicity and environmental concerns,<sup>14</sup> have thus far prevented perovskite solar cells from joining the more established commercial thin-film PV technologies, such as cadmium telluride (CdTe) and copper indium gallium diselenide (CIGS). Particularly, the lack of durability and inconsistent power generation are the most critical technical issues to be addressed before the full potential of perovskite PV technology can be fulfilled. With the rapid advances of perovskite PV technology, fundamental understanding of perovskite materials enables crucial insights in support of overcoming the remaining challenges.

Methylammonium lead iodide ( $\text{MAPbI}_3$ ) with a band gap of  $\sim 1.60$  eV<sup>15</sup> is the prototypical perovskite light-absorbing material that was developed at the early stage and since then has been extensively studied as the benchmark absorber layer in single-junction perovskite solar cells. The advances in perovskite PV technology were enabled by incorporating formamidinium (FA) to the perovskite composition to make mixed cation  $\text{MA}_{1-x}\text{FA}_x\text{PbI}_3$  perovskites, which extends the absorption edge to longer wavelengths and enhances the

optoelectronic properties (e.g., carrier lifetime, diffusion length) of perovskites,<sup>16</sup> resulting in PCEs ( $>23\%$ )<sup>17</sup> higher than the  $\sim 21\%$  seen for pure  $\text{MAPbI}_3$ .<sup>18</sup> Despite the enhanced device performance, the intrinsic structural and optoelectronic properties of  $\text{MA}_{1-x}\text{FA}_x\text{PbI}_3$  (e.g., crystal phase transformation, nature of the defects) that govern device performance and stability have yet to be fully explored. Particularly, investigating the temperature-dependent crystal phase transformation and the optoelectronic properties of  $\text{MA}_{1-x}\text{FA}_x\text{PbI}_3$  perovskite at low temperatures allows for the understanding of not only the fundamental semiconductor behaviors of  $\text{MA}_{1-x}\text{FA}_x\text{PbI}_3$  perovskites but also the device physics of perovskite solar cells. Furthermore, exploring the optoelectronic properties of  $\text{MA}_{1-x}\text{FA}_x\text{PbI}_3$  over a wide range of temperatures and particularly at low temperatures is of interest for their potential use in space power applications.

With these considerations, in situ photoluminescence (PL) spectroscopy has been employed to study the structural and optoelectronic properties and phase stability of  $\text{MAPbI}_3$  perovskites.<sup>19–21</sup> Particularly for low-temperature PL measurements, Dar et al. have revealed the coexistence of both orthorhombic and tetragonal phases in  $\text{MAPbI}_3$  utilizing low temperature PL,<sup>22</sup> whereas other reports correlated PL signals based on the first-order thermodynamic phase transition of  $\text{MAPbI}_3$  that occurs at  $\sim 160$  K.<sup>22,23</sup> Phuyong et al. observed exciton and free carrier emissions in polycrystalline  $\text{MAPbI}_3$

Received: November 1, 2019

Accepted: December 9, 2019

Published: December 10, 2019

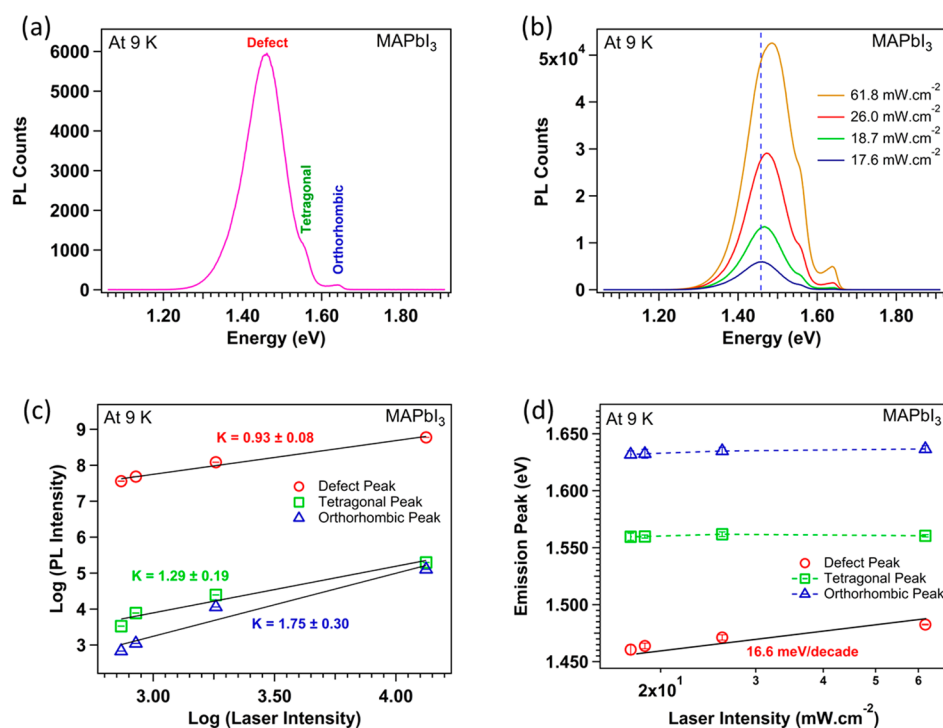


**Figure 1.** (a) PL spectrum of MAPbI<sub>3</sub> at 9 K (at 17.6 mW·cm<sup>-2</sup>) and (b) PL spectra at various laser excitation intensities. (c) Integrated PL and (d) emission peak energy vs laser intensity for three PL peaks observed for MAPbI<sub>3</sub>.

thin films at low temperatures.<sup>24</sup> Such photophysics in perovskites at various temperatures (and within the corresponding phases) contributes to the understanding of photoexcited charge carriers and may lead to improved stability and power conversion efficiency for MAPbI<sub>3</sub> and MA<sub>1-x</sub>FA<sub>x</sub>PbI<sub>3</sub> solar cells.

Low-temperature PL measurement can be used to investigate the defects presented in semiconductors. Intrinsic defects, such as lattice dislocations, grain boundaries (GBs), surface/interface, and point defects, may trap photoexcited charge carriers, leading to nonradiative recombination, reduced carrier lifetime, and inhibited solar cell performance. Yang et al. theoretically reported the presence of charge compensating iodine vacancy (V<sub>I</sub>) donors and methylammonium vacancy (V<sub>MA</sub>) acceptors in MAPbI<sub>3</sub>.<sup>25</sup> An important consequence of charge compensating defects in MAPbI<sub>3</sub> is that the final free carrier concentration often ends up very low. Such challenges in controlling doping lead furthermore to near-intrinsic MAPbI<sub>3</sub> behavior. Therefore, identification of defects and their behaviors at various temperatures is essential to understand and control the intrinsic and extrinsic doping, which in turn play a significant role in transport and contact performance of the final PV devices.

Here, we report the properties of intrinsic defects in polycrystalline MA<sub>1-x</sub>FA<sub>x</sub>PbI<sub>3</sub> films discovered via temperature dependent PL spectroscopy from 9 to 290 K. Note that lead thiocyanate [Pb(SCN)<sub>2</sub>] additive was incorporated into the perovskite films due to its beneficial impact on enlarged grain size and passivation of GBs and thus also to enhance the PCE of the resulting perovskite solar cells.<sup>16,26</sup> We observed PL peaks corresponding to orthorhombic and tetragonal phases of MAPbI<sub>3</sub> at 9 K. More interestingly, a band-tail related defect-assisted transition peak was observed in MAPbI<sub>3</sub>, which was rarely reported previously in the literature. Furthermore, we showed that the substitution of MA by FA at the appropriate

concentration within MAPbI<sub>3</sub> suppresses the formation of such defect states and slows the phase transformation.

Photoluminescence spectroscopy is one powerful technique to study defect related sub-band gap luminescence emission in semiconductors. Typically, temperature and laser excitation intensity dependent PL studies are combined to identify the nature of observed emission peaks in the spectrum. The variations in temperature and excitation intensity alter the thermal energy and the population of photogenerated charge carriers and thereby determine the charge carriers' propensity to occupy either long-lived radiative defect sites or short-lived nonradiative recombination sites. Figure 1 shows the results of laser excitation intensity dependent PL spectra of a MAPbI<sub>3</sub> film measured at 9 K. Figure 1a shows a typical PL spectrum containing three emission peaks at 1.46, 1.56, and 1.65 eV, respectively. In contrast to most reports in the literature with the most intense peaks at 1.55–1.65 eV,<sup>20,21,27</sup> our measurement shows that the PL emission of MAPbI<sub>3</sub> at low temperatures is dominated by low energy emission at 1.46 eV. To further investigate the nature of these observed emission bands, laser excitation intensity dependent PL spectra were acquired (Figure 1b). For a semiconductor material, integrated PL intensity ( $I_{PL}$ ) typically follows a power law,  $I_{PL} = I_{laser}^k$ , where  $I_{laser}$  is laser intensity, and  $k$  is the exponent. For band-to-band (BB) and excitonic recombination,  $k$  falls in the range of 1 to 2, whereas for defect assisted transitions [e.g., free-to-bound (FB) and donor-to-acceptor (DAP) recombination],  $k$  is less than 1.<sup>28–30</sup> Through power fitting of laser intensity dependent PL data (Figure 1c), we obtained  $k = 0.93$ , 1.29, and 1.75 values for the peaks at 1.46, 1.56, and 1.65 eV, respectively, indicating that the 1.46 eV peak represents a defect assisted transition, whereas the 1.56 and 1.65 eV peaks correspond to excitonic emissions. The exciton peaks at 1.56 and 1.65 eV correspond to the tetragonal ( $I4/mcm$ ) and orthorhombic ( $Pnma$ ) phases of MAPbI<sub>3</sub>, respectively. Note

that the higher  $k$  value for the orthorhombic phase than the tetragonal phase shows stronger exciton characteristics in the orthorhombic phase, consistent with the reports that both exciton and free carrier features exist in low-temperature PL of MAPbI<sub>3</sub>.<sup>31</sup> Additionally, the coexistence of orthorhombic and tetragonal phases in perovskites has been reported elsewhere.<sup>20,32,33</sup>

Figure 1d plots the variations in the peak locations as a function of laser excitation intensity. The peak locations of the two exciton emission bands remain constant with increasing laser intensity. In contrast, the defect peak at 1.46 eV blue-shifted with an increase in laser intensity at 16.6 meV/decade. Such a large blue-shift (aka,  $j$ -shift) is the characteristic of a band-tail (BT) related transition, which is widely present in copper chalcogenide semiconductors (e.g., CuInSe<sub>2</sub> and Cu<sub>2</sub>ZnSnS<sub>4</sub>) possessing a large number of charge compensating defect states.<sup>34–36</sup> In highly compensating semiconductors consisting of similar amounts of donor and acceptor defects, electrons from the donor sites recombine with holes localized at the acceptor sites, leading to the coexistence of positively charged donors and negatively charged acceptors at various locations. As a result, spatially distributed charged regions establish the fluctuating potential of the valence band and conduction band edges.<sup>37</sup> The potential fluctuations arising from such charged defect states form localized trap states within the band gap, resulting in the large  $j$ -shift.<sup>36</sup> At high laser excitation intensity, the increased concentration of free carriers effectively screens the electrostatic potential of the charged defects. This charge screening effect results in flattening of the potential fluctuation causing a blue shift of the defect peak.<sup>37,38</sup> Figure 2a represents the schematic of the

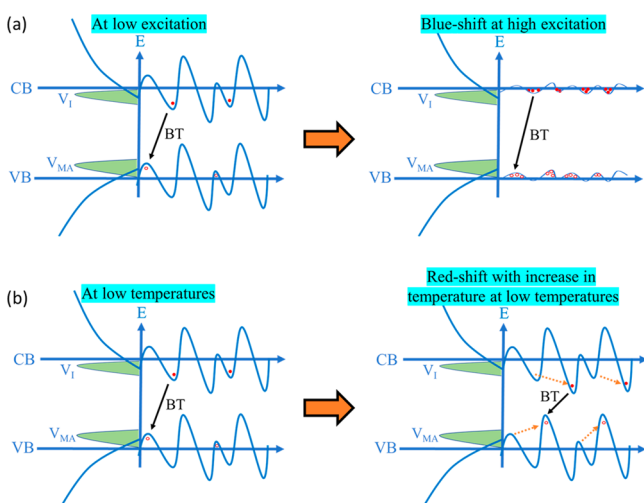


**Figure 2.** Schematic illustration of band fluctuation in MAPbI<sub>3</sub>. (a) Flattening of band-tail at high laser excitation intensity causing blue-shift of band-tail related defect peak in MAPbI<sub>3</sub>. (b) Carriers occupying lower energy states at the band-tail states with an increase in thermal energy at low temperatures causing red-shift of band-tail related defect peak in MAPbI<sub>3</sub>.

flattening of the band-tail arising from high laser excitation intensity. Despite rarely being reported for low-temperature PL measurements, the existence of compensating  $V_I$  donors and  $V_{MA}$  acceptors in MAPbI<sub>3</sub> has been reported by previous researchers.<sup>25,39</sup> Due to the high vapor pressures of its decomposition products, MAPbI<sub>3</sub> is prone to loss of MA and I components in the forms of methylamine and hydrogen

iodide gases,<sup>40</sup> resulting in the formation of compensating  $V_I$  and  $V_{MA}$  defects during the preparation and transfer of the sample. It is also worth noting that intense light emission can lead to the photoinduced decomposition of MAPbI<sub>3</sub>.<sup>41</sup> Particularly for polycrystalline MAPbI<sub>3</sub> thin films, these defects are likely to form at the surface and GBs. As a consequence, these charge-compensating donor and acceptor defects in MAPbI<sub>3</sub> limit the carrier concentration and thus lead to the intrinsic resistive nature of MAPbI<sub>3</sub>. Note that in this study Pb(SCN)<sub>2</sub> additive was incorporated into the MAPbI<sub>3</sub> film, resulting in large grain size and better crystallinity (Figures S1 and S2). The PL emission of the MAPbI<sub>3</sub> film with Pb(SCN)<sub>2</sub> is more pronounced than that of the film without Pb(SCN)<sub>2</sub>, as shown in Figure S3, likely due to enhanced crystallinity and reduced nonradiative recombination.

The PL emission features of MAPbI<sub>3</sub> were further investigated via temperature dependent PL. Figure 3a,b, respectively, show the temperature dependent PL spectra of MAPbI<sub>3</sub> and the corresponding peak shift as a function of temperature. The defect peak (1.46 eV at 9 K) red-shifted between 9 and 80 K and then blue-shifted above 80 K before disappearing near 130 K. The red-shift of a PL peak followed by the blue-shift at low temperatures with an increase in thermal energy is typically observed in semiconductors with charge compensating defects,<sup>36,38,42</sup> which further confirms that the 1.46 eV defect emission is the consequence of a BT transition. The red-shift is related to the thermal energy of localized charge carriers. At low temperatures, an increase in thermal energy associated with the rising sample temperature allows the localized charge carriers to overcome local potential barriers and move to the nearby lower-potential sites (Figure 2b). As a result of charge redistribution to lower energy states, the quasi-Fermi levels move toward the center of the band gap, lowering the peak energy of the BT band.<sup>37</sup> The nature of the blue-shift evident for  $T > 80$  K is attributed to thermal activation of defect-bound holes back to the valence band.<sup>36</sup> The defect peak disappeared when the temperature was above 130 K due to the trap filling of the BT states by thermalized charge carriers, indicating that the density of defect states in the BT is low, which may be a reason that the defect PL emission has rarely been reported in the literature.

The PL emission peak (1.65 eV at 9 K) arising from the orthorhombically structured domains showed a blue shift with increasing temperature, in opposition to the well-known Varshni relation in which the band gap of a typical semiconductor exhibits a red shift with increasing temperature.<sup>43</sup> The origin of the abnormal band gap shift with respect to temperature is likely related to the spin–orbit coupling enhanced electron–phonon interaction.<sup>44,45</sup> The orthorhombic peak disappeared at  $\sim 150$  K, indicating a full conversion to the tetragonal phase. In contrast, the tetragonal peak (1.56 eV at 9 K) first blue-shifted until 100 K and then red-shifted up to 160 K. It has been noted here that above 150 K, there evolves only one emission peak representing tetragonal phase of MAPbI<sub>3</sub>, which confirms that the first order phase transition in MAPbI<sub>3</sub> occurs at  $\sim 150$  K. This phase transition has been observed and attributed to the dynamic order–disorder arrangement of MA cations and the inorganic PbI<sub>6</sub> octahedral framework.<sup>9</sup> Figure 3b shows the evolution of two different phases as well as the first order phase transition temperature ( $\sim 150$  K) in MAPbI<sub>3</sub> perovskite.

To gain further insight into the observed defect peak, we obtained PL dynamics utilizing time-resolved PL. Photoexcited

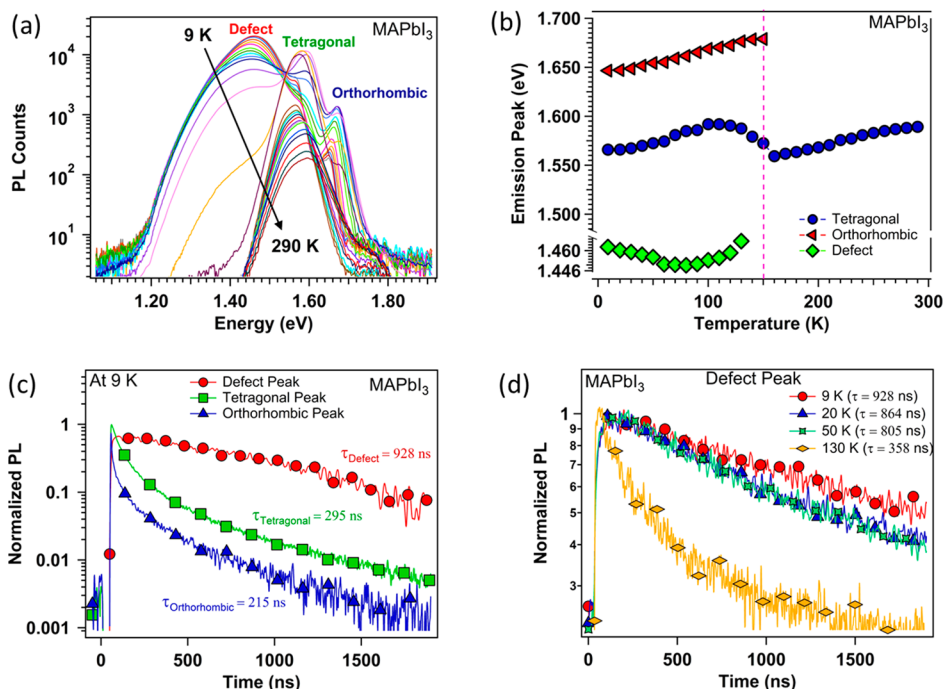


**Figure 3.** (a) Evolution of PL spectra and (b) different phases of MAPbI<sub>3</sub> revealed by temperature dependent PL. (c) PL decays of MAPbI<sub>3</sub> corresponding to different peaks at 9 K. (d) PL dynamics of MAPbI<sub>3</sub> at the defect site as a function of temperature.

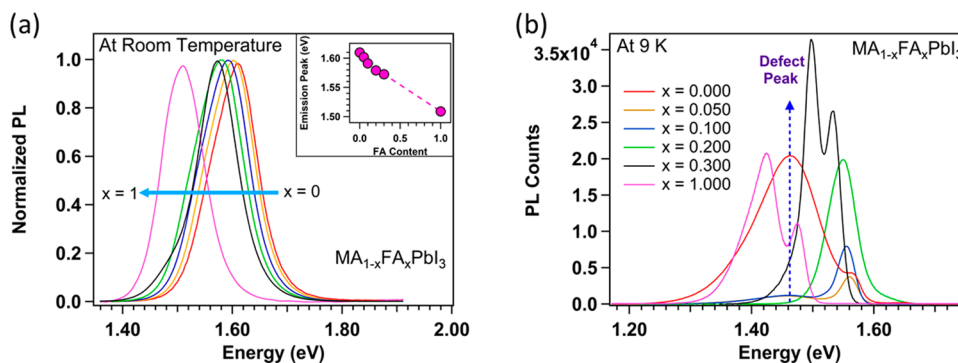


**Figure 4.** PL spectra of MA<sub>1-x</sub>FA<sub>x</sub>PbI<sub>3</sub> as a function of FA concentration acquired at (a) room temperature and (b) 9 K.

carriers are found to be long-lived at defect sites with a mean carrier lifetime of  $\sim 928$  ns compared to the excitons (mean lifetimes of 215 and 295 ns, respectively, for orthorhombic and tetragonal peaks), as depicted in Figure 3c. The increased carrier lifetime at defect sites can be attributed to the localization of carriers at band-tails before recombination.<sup>46</sup> However, the band-tail recombination lifetime decreases with increasing temperature due to the delocalization of carriers at band-tails driven by higher thermal energy, as depicted in Figure 3d. Furthermore, we found that the exciton lifetime (215 to 295 ns) at 9 K is significantly shorter than that (470 ns) we reported previously for MAPbI<sub>3</sub> at room temperature.<sup>16</sup> The reduced nonadiabatic electron–phonon coupling and shortened decoherence time are the reason behind longer carrier lifetime of MAPbI<sub>3</sub> at a high temperature compared to that at a low temperature.<sup>47</sup>

To explore the influence of the organic cation composition on the observed defect peak in MAPbI<sub>3</sub>, we have carried out PL measurements of mixed cation MA<sub>1-x</sub>FA<sub>x</sub>PbI<sub>3</sub> at room temperature and 9 K for  $x$  ranging from 0 to 1. It is known that FA incorporation into MAPbI<sub>3</sub> narrows its band gap and

increases carrier lifetimes, thereby resulting in enhanced performance of MA<sub>1-x</sub>FA<sub>x</sub>PbI<sub>3</sub> solar cells.<sup>16</sup> The defect analysis of MA<sub>1-x</sub>FA<sub>x</sub>PbI<sub>3</sub> perovskite film is crucial to understanding the origins of the improved optoelectronic properties. PL spectra taken at room temperature (Figure 4a) show the band gap dependence on FA concentration. Increasing FA content ( $x$ ) from 0 to 1 leads to a decrease in band gap from 1.61 to 1.51 eV, as shown in the inset of Figure 4a.

Interestingly, PL spectra acquired at 9 K (Figure 4b) show that the PL intensity of defect emission ( $\sim 1.46$  eV) is greatly quenched with the incorporation of even a small amount (5%) of FA, and that the defect emission vanishes for  $x \geq 0.2$ . The suppression of intrinsic defects in organic–inorganic metal halide perovskite using mixed cations has also been reported by Liu and Yam.<sup>48</sup> One possible reason for the gradual diminishing and disappearance of the band-tail related defect peak could be the reduction of the V<sub>MA</sub> vacancies by FA inclusion. Detailed investigations are ongoing.

For further confirmation, observed peaks in MA<sub>1-x</sub>FA<sub>x</sub>PbI<sub>3</sub> for  $x = 0.2$  and  $x = 0.3$  were carefully studied by applying laser intensity dependent PL measurement at 15 K, as shown in

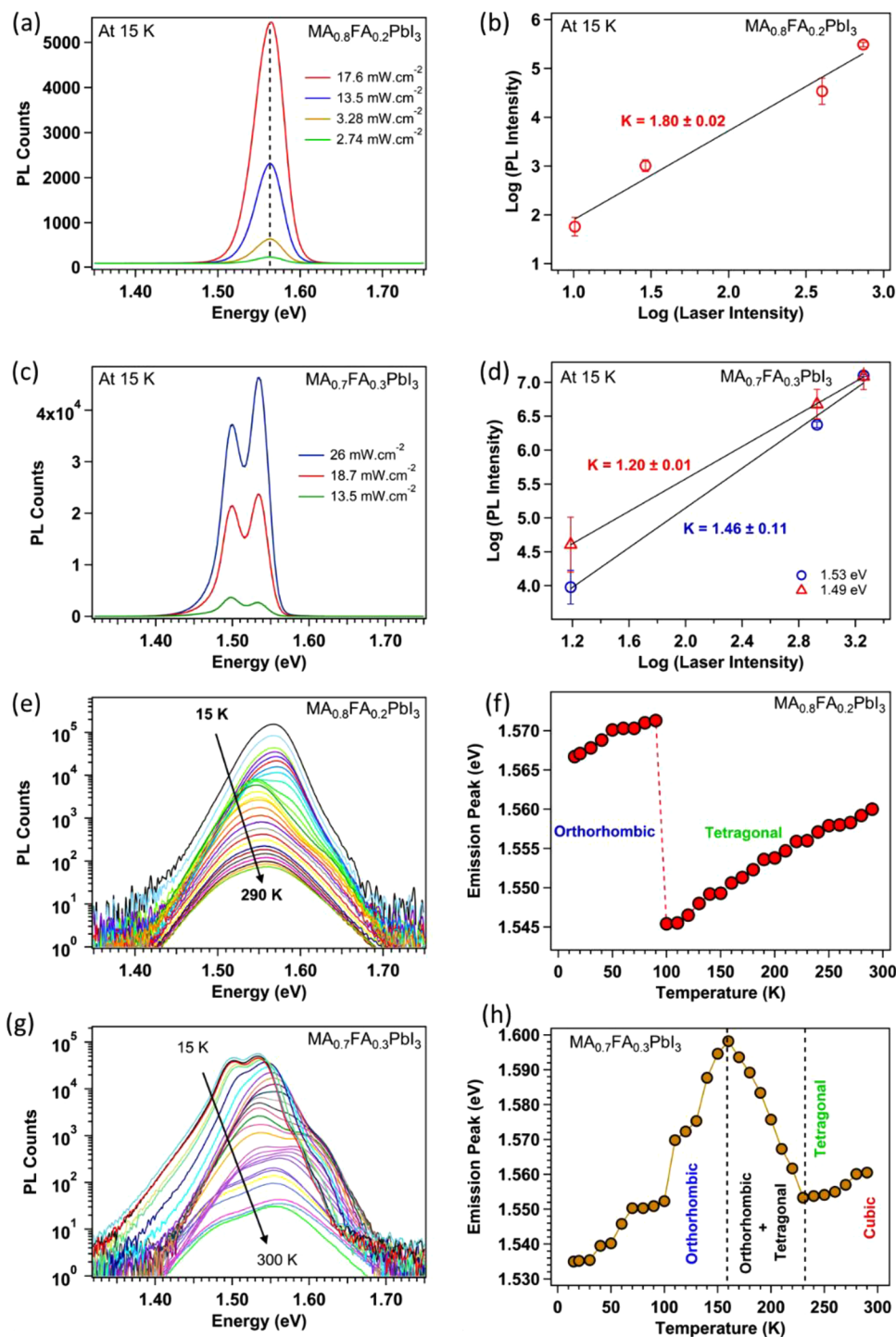


**Figure 5.** (a) PL spectra of  $\text{MA}_{0.8}\text{FA}_{0.2}\text{PbI}_3$  at various laser intensities and (b) PL intensity vs laser intensity. (c) PL spectra of  $\text{MA}_{0.7}\text{FA}_{0.3}\text{PbI}_3$  at various laser intensities and (d) PL intensity vs laser intensity. (e) Evolution of PL spectra and (f) different phases of  $\text{MA}_{0.8}\text{FA}_{0.2}\text{PbI}_3$  revealed by temperature dependent PL. (g) Evolution of PL spectra and (h) different phases of  $\text{MA}_{0.7}\text{FA}_{0.3}\text{PbI}_3$  revealed by temperature dependent PL.

Figure 5a,c. Interestingly,  $\text{MA}_{0.2}\text{FA}_{0.8}\text{PbI}_3$  shows a single peak located at  $\sim 1.56$  eV, whereas  $\text{MA}_{0.3}\text{FA}_{0.7}\text{PbI}_3$  shows dual-peak emission at 1.49 and 1.53 eV. All these peaks show  $k > 1$  for the emission–excitation intensity relationship, as shown in Figure 5b,d, indicating exciton behaviors. The origin of the distinct dual-peak emission in  $\text{MA}_{0.3}\text{FA}_{0.7}\text{PbI}_3$  is still unclear. It may originate from the nanodomains of different phases<sup>49</sup> or interactions between excitons and phonons<sup>50</sup> or polarons.<sup>51</sup> Similar behaviors were observed in the laser intensity and

temperature dependent PL results of pristine  $\text{FAPbI}_3$  ( $x = 1.0$ ) (Figures S4 and S5). Since no defect peak was observed in  $\text{MA}_{1-x}\text{FA}_x\text{PbI}_3$  for  $x \geq 0.2$ , here we confirm that mixing an appropriate amount of FA in  $\text{MAPbI}_3$  can suppress the formation of charged defect states in  $\text{MAPbI}_3$ .

Furthermore, we have studied the impact of FA inclusion on the crystal phase of  $\text{MA}_{1-x}\text{FA}_x\text{PbI}_3$  via temperature dependent PL (Figure 5e,g). Like  $\text{MAPbI}_3$ , orthorhombic to tetragonal phase transformation is first order (Type-I) in the case of

MA<sub>0.8</sub>FA<sub>0.2</sub>PbI<sub>3</sub>, while further increase in the FA concentration to  $x = 0.3$  was found to slow down the phase transformation, resulting in a Type-II transition as shown in Figure 5f,h. Since the geometry and symmetry of FA<sup>+</sup> are more flexible than those of MA<sup>+</sup>, the addition of FA into MAPbI<sub>3</sub> lowers the lattice distortions, particularly at low temperatures.<sup>52,53</sup> Such a reduced lattice distortion may be attributed to type-II phase transition in MA<sub>0.7</sub>FA<sub>0.3</sub>PbI<sub>3</sub>.

In summary, low temperature PL analysis has been performed on polycrystalline MA<sub>1-x</sub>FA<sub>x</sub>PbI<sub>3</sub> films. Our analysis reveals the existence of charge compensating defects in MAPbI<sub>3</sub> at low temperatures, which may describe the intrinsic nature of MAPbI<sub>3</sub> perovskite. More interestingly, we observe that FA inclusion results in the suppression of charged defect PL emission. Additionally, incorporation of FA into MAPbI<sub>3</sub> slows down the phase transformation (orthorhombic to tetragonal). The detailed defect analysis and phase transformation information revealed by our PL and TRPL studies may be beneficial in improving the optoelectronic properties of organo-metal halide perovskites and the performance of their PV devices.

## EXPERIMENTAL DETAILS

**Perovskite Precursor Solution Preparation.** The MAPbI<sub>3</sub> perovskite precursor solution was prepared by dissolving 1.43 M equimolar lead iodide (PbI<sub>2</sub>, Alfa Aesar, 99.9985%) and methylammonium iodide (MAI, Greatcell Solar) in *N,N*-dimethylformamide (DMF) and dimethyl sulfoxide (DMSO) (volume ratio = 9:1). A small amount (3% molar ratio to PbI<sub>2</sub>) of lead thiocyanate [Pb(SCN)<sub>2</sub>, Sigma-Aldrich, 99.5%] was added into the precursor solution as an additive.<sup>54</sup> The FAPbI<sub>3</sub> precursor solution was prepared by dissolving 1.43 M equimolar PbI<sub>2</sub> (Alfa Aesar, 99.9985%) and formamidinium iodide (FAI, Greatcell Solar) in mixed DMF/DMSO (volume ratio = 9:1). The MA<sub>1-x</sub>FA<sub>x</sub>PbI<sub>3</sub> perovskite precursor was prepared by mixing the desired quotas of MAPbI<sub>3</sub> and FAPbI<sub>3</sub> solution.

**Perovskite Film Preparation.** The perovskite precursor solution was filtered using a 0.45 mm PTFE filter and dripped onto soda-lime glass substrates. The solution was spin-coated at 500 rpm for 3 s and 4000 rpm for 60 s. At ~8 s of the second spin step, 700  $\mu$ L of diethyl ether was dripped on the spinning substrate. The coated substrates were then annealed at 60 °C for 2 min and 100 °C for 5 min in a nitrogen glovebox.

**PL Characterization.** For steady-state PL, a 532 nm continuous wave laser beam (beam diameter ~90  $\mu$ m) was used for the photoexcitation. Temperature dependent PL measurements were carried out by mounting the sample on the coldfinger of a He closed-cycle refrigerator cryostat system from Advanced Research Systems. PL signal was detected by a Horiba Symphony-II CCD (charged coupled device) detector after a 300 g/mm grating monochromator. PL measurements were performed using laser intensity in the range of ~2.74 to 61.8 mW·cm<sup>-2</sup>. TRPL measurements were carried out utilizing time correlated single photon counting module (TCSPC). Samples were illuminated by a 532 nm pulsed laser (pulse width = 5 ps, beam diameter ~150  $\mu$ m) at  $1.4 \times 10^{10}$  photons·pulse<sup>-1</sup>·cm<sup>-2</sup>. Radiative recombination events were detected by APD/PMT hybrid detector (integration time = 300 s). TCSPC decay curves obtained in TRPL measurement were fitted by iterative deconvolution with the measured system response function.

## ASSOCIATED CONTENT

### Supporting Information

The Supporting Information is available free of charge at <https://pubs.acs.org/doi/10.1021/acs.jpcllett.9b03234>.

XRD patterns and SEM images of MA<sub>x</sub>FA<sub>1-x</sub>PbI<sub>3</sub> with Pb(SCN)<sub>2</sub> additive, low temperature PL spectra of MAPbI<sub>3</sub> with or without Pb(SCN)<sub>2</sub> additive, and laser power and temperature dependent PL spectra of FAPbI<sub>3</sub> (PDF)

## AUTHOR INFORMATION

### Corresponding Author

\*Email: [randy.ellingson@utoledo.edu](mailto:randy.ellingson@utoledo.edu).

### ORCID

Niraj Shrestha: 0000-0001-5702-2938

Zhaoning Song: 0000-0002-6677-0994

Ebin Bastola: 0000-0002-4194-3385

Xiaoming Wang: 0000-0002-5438-1334

Yanfa Yan: 0000-0003-3977-5789

Randy J. Ellingson: 0000-0001-9520-6586

### Author Contributions

#N.S. and Z.S. contributed equally to this work.

### Notes

The views and conclusions contained herein are those of the authors and should not be interpreted as necessarily representing the official policies or endorsements, either expressed or implied, of Air Force Research Laboratory or the U.S. Government.

The authors declare no competing financial interest.

## ACKNOWLEDGMENTS

This work is supported by National Science Foundation (NSF) under contract no. EECs-1665172, Office of Naval Research under contract no. N00014-17-1-2223, and Air Force Research Laboratory under agreement number FA9453-18-2-0037. The U.S. Government is authorized to reproduce and distribute reprints for Governmental purposes notwithstanding any copyright notation thereon.

## REFERENCES

- (1) Saidaminov, M. I.; Abdelhady, A. L.; Murali, B.; Alarousu, E.; Burlakov, V. M.; Peng, W.; Dursun, I.; Wang, L.; He, Y.; Maculan, G.; et al. High-quality Bulk Hybrid Perovskite Single Crystals within Minutes by Inverse Temperature Crystallization. *Nat. Commun.* **2015**, *6*, 7586.
- (2) Park, N.-G. Perovskite Solar Cells: An Emerging Photovoltaic Technology. *Mater. Today* **2015**, *18* (2), 65–72.
- (3) Dong, Q.; Fang, Y.; Shao, Y.; Mulligan, P.; Qiu, J.; Cao, L.; Huang, J. Electron-hole Diffusion Lengths > 175 nm in Solution-grown CH<sub>3</sub>NH<sub>3</sub>PbI<sub>3</sub> Single Crystals. *Science* **2015**, *347* (6225), 967–970.
- (4) Miyata, A.; Mitioglu, A.; Plochocka, P.; Portugall, O.; Wang, J. T.-W.; Stranks, S. D.; Snaith, H. J.; Nicholas, R. J. Direct Measurement of the Exciton Binding Energy and Effective Masses for Charge Carriers in Organic-inorganic Tri-halide Perovskites. *Nat. Phys.* **2015**, *11* (7), 582–587.
- (5) Jung, H. S.; Han, G. S.; Park, N.-G.; Ko, M. J. Flexible Perovskite Solar Cells. *Joule* **2019**, *3* (8), 1850–1880.
- (6) Song, Z.; McElvany, C. L.; Phillips, A. B.; Celik, I.; Krantz, P. W.; Wathage, S. C.; Liyanage, G. K.; Apul, D.; Heben, M. J. A Technoeconomic Analysis of Perovskite Solar Module Manufacturing with Low-cost Materials and Techniques. *Energy Environ. Sci.* **2017**, *10* (6), 1297–1305.

- (7) NREL <https://www.nrel.gov/pv/assets/images/efficiency-chart.png>.
- (8) Bisquert, J.; Juarez-Perez, E. J. The Causes of Degradation of Perovskite Solar Cells. *J. Phys. Chem. Lett.* **2019**, *10* (19), 5889–5891.
- (9) Park, B.-w.; Seok, S. I. Intrinsic Instability of Inorganic–organic Hybrid Halide Perovskite Materials. *Adv. Mater.* **2019**, *31* (20), 1805337.
- (10) Roose, B.; Wang, Q.; Abate, A. The Role of Charge Selective Contacts in Perovskite Solar Cell Stability. *Adv. Energy Mater.* **2018**, *9* (5), 1803140.
- (11) Zhang, H.; Nazeeruddin, M. K.; Choy, W. C. H. Perovskite Photovoltaics: The Significant Role of Ligands in Film Formation, Passivation, and Stability. *Adv. Mater.* **2019**, *31* (8), 1805702.
- (12) Huang, F.; Li, M.; Siffalovic, P.; Cao, G.; Tian, J. From Scalable Solution Fabrication of Perovskite Films Towards Commercialization of Solar Cells. *Energy Environ. Sci.* **2019**, *12* (2), 518–549.
- (13) Chen, B.; Yang, M.; Priya, S.; Zhu, K. Origin of J–V Hysteresis in Perovskite Solar Cells. *J. Phys. Chem. Lett.* **2016**, *7* (5), 905–917.
- (14) Celik, I.; Song, Z.; Cimaroli, A. J.; Yan, Y.; Heben, M. J.; Apul, D. Life Cycle Assessment (LCA) of Perovskite PV Cells Projected From Lab to Fab. *Sol. Energy Mater. Sol. Cells* **2016**, *156*, 157–169.
- (15) Jung, H. S.; Park, N.-G. Perovskite Solar Cells: From Materials to Devices. *Small* **2015**, *11* (1), 10–25.
- (16) Wang, C.; Zhao, D.; Yu, Y.; Shrestha, N.; Grice, C. R.; Liao, W.; Cimaroli, A. J.; Chen, J.; Ellingson, R. J.; Zhao, X.; Yan, Y. Compositional and Morphological Engineering of Mixed Cation Perovskite Films for Highly Efficient Planar and Flexible Solar Cells with Reduced Hysteresis. *Nano Energy* **2017**, *35*, 223–232.
- (17) Jiang, Q.; Zhao, Y.; Zhang, X.; Yang, X.; Chen, Y.; Chu, Z.; Ye, Q.; Li, X.; Yin, Z.; You, J. Surface Passivation of Perovskite Film for Efficient Solar Cells. *Nat. Photonics* **2019**, *13* (7), 460–466.
- (18) Deng, Y.; Zheng, X.; Bai, Y.; Wang, Q.; Zhao, J.; Huang, J. Surfactant-controlled Ink Drying Enables High-Speed Deposition of Perovskite Films for Efficient Photovoltaic Modules. *Nature Energy* **2018**, *3* (7), 560–566.
- (19) Song, Z.; Shrestha, N.; Waththage, S. C.; Liyanage, G. K.; Almutawah, Z. S.; Ahangharnejhad, R. H.; Phillips, A. B.; Ellingson, R. J.; Heben, M. J. Impact of Moisture on Photoexcited Charge Carrier Dynamics in Methylammonium Lead Halide Perovskites. *J. Phys. Chem. Lett.* **2018**, *9* (21), 6312–6320.
- (20) Liu, Y.; Lu, H.; Niu, J.; Zhang, H.; Lou, S.; Gao, C.; Zhan, Y.; Zhang, X.; Jin, Q.; Zheng, L. Temperature-dependent Photoluminescence Spectra and Decay Dynamics of MAPbBr<sub>3</sub> and MAPbI<sub>3</sub> Thin Films. *AIP Adv.* **2018**, *8* (9), 095108.
- (21) Kong, W.; Ye, Z.; Qi, Z.; Zhang, B.; Wang, M.; Rahimi-Iman, A.; Wu, H. Characterization of an Abnormal Photoluminescence Behavior upon Crystal-phase Transition of Perovskite CH<sub>3</sub>NH<sub>3</sub>PbI<sub>3</sub>. *Phys. Chem. Chem. Phys.* **2015**, *17* (25), 16405–16411.
- (22) Dar, M. I.; Jacopin, G.; Meloni, S.; Mattoni, A.; Arora, N.; Boziki, A.; Zakeeruddin, S. M.; Rothlisberger, U.; Grätzel, M. Origin of Unusual Bandgap Shift and Dual Emission in Organic-Inorganic Lead Halide Perovskites. *Science Advances* **2016**, *2*, e1601156.
- (23) Baikie, T.; Fang, Y.; Kadro, J. M.; Schreyer, M.; Wei, F.; Mhaisalkar, S. G.; Graetzel, M.; White, T. J. Synthesis and Crystal Chemistry of the Hybrid Perovskite CH<sub>3</sub>NH<sub>3</sub>PbI<sub>3</sub> for Solid-state Sensitized Solar Cell Applications. *J. Mater. Chem. A* **2013**, *1* (18), 5628–5641.
- (24) Phuong, L. Q.; Yamada, Y.; Nagai, M.; Maruyama, N.; Wakamiya, A.; Kanemitsu, Y. Free Carriers versus Excitons in CH<sub>3</sub>NH<sub>3</sub>PbI<sub>3</sub> Perovskite Thin Films at Low Temperatures: Charge Transfer from the Orthorhombic Phase to the Tetragonal Phase. *J. Phys. Chem. Lett.* **2016**, *7* (13), 2316–2321.
- (25) Yang, J.-H.; Yin, W.-J.; Park, J.-S.; Wei, S.-H. Self-regulation of Charged Defect Compensation and Formation Energy Pinning in Semiconductors. *Sci. Rep.* **2015**, *5*, 16977.
- (26) Ke, W.; Xiao, C.; Wang, C.; Saparov, B.; Duan, H.-S.; Zhao, D.; Xiao, Z.; Schulz, P.; Harvey, S. P.; Liao, W.; et al. Employing Lead Thiocyanate Additive to Reduce the Hysteresis and Boost the Fill Factor of Planar Perovskite Solar Cells. *Adv. Mater.* **2016**, *28* (26), 5214–5221.
- (27) Milot, R. L.; Eperon, G. E.; Snaith, H. J.; Johnston, M. B.; Herz, L. M. Temperature-dependent Charge-carrier Dynamics in CH<sub>3</sub>NH<sub>3</sub>PbI<sub>3</sub> Perovskite Thin Films. *Adv. Funct. Mater.* **2015**, *25* (39), 6218–6227.
- (28) Schmidt, T.; Daniel, G.; Lischka, K. The Excitation Power Dependence of the Near Band Edge Photoluminescence of II-VI Semiconductors. *J. Cryst. Growth* **1992**, *117* (1), 748–752.
- (29) Krustok, J.; Valdna, V.; Hjelt, K.; Collan, H. Deep Center Luminescence in P-type CdTe. *J. Appl. Phys.* **1996**, *80* (3), 1757–1762.
- (30) Roland, P. J.; Paudel, N. R.; Chuanxiao, X.; Yan, Y.; Ellingson, R. J. Photoluminescence Spectroscopy of Cadmium Telluride Deep Defects, *2014 IEEE 40th Photovoltaic Specialist Conference (PVSC)*, 8–13 June; IEEE, 2014; pp 3266–3271.
- (31) Shi, J.; Zhang, H.; Li, Y.; Jasieniak, J. J.; Li, Y.; Wu, H.; Luo, Y.; Li, D.; Meng, Q. Identification of High-temperature Exciton States and Their Phase-dependent Trapping Behaviour in Lead Halide Perovskites. *Energy Environ. Sci.* **2018**, *11* (6), 1460–1469.
- (32) Yamada, Y.; Nakamura, T.; Endo, M.; Wakamiya, A.; Kanemitsu, Y. Near-band-edge Optical Responses of Solution-processed Organic–inorganic Hybrid Perovskite CH<sub>3</sub>NH<sub>3</sub>PbI<sub>3</sub> on Mesoporous TiO<sub>2</sub> electrodes. *Appl. Phys. Express* **2014**, *7* (3), 032302.
- (33) Panzer, F.; Baderschneider, S.; Gujar, T. P.; Unger, T.; Bagnich, S.; Jakoby, M.; Bäessler, H.; Hüttner, S.; Köhler, J.; Moos, R.; et al. Reversible Laser-induced Amplified Spontaneous Emission from Coexisting Tetragonal and Orthorhombic Phases in Hybrid Lead Halide Perovskites. *Adv. Opt. Mater.* **2016**, *4* (6), 917–928.
- (34) Krustok, J.; Jagomägi, A.; Grossberg, M.; Raudoja, J.; Danilson, M. Photoluminescence Properties of Polycrystalline AgGaTe<sub>2</sub>. *Sol. Energy Mater. Sol. Cells* **2006**, *90* (13), 1973–1982.
- (35) Shrestha, N.; Sapkota, D. R.; Subedi, K. K.; Pradhan, P.; Koirala, P.; Phillips, A. B.; Collins, R. W.; Heben, M. J.; Ellingson, R. J. Identification of Defect Levels in Copper Indium Diselenide (CuInSe<sub>2</sub>) Thin Films via Photoluminescence Studies. *MRS Advances* **2018**, *3* (52), 3135–3141.
- (36) Yakushev, M. V.; Krustok, J.; Grossberg, M.; Volkov, V. A.; Mudryi, A. V.; Martin, R. W. A Photoluminescence Study of CuInSe<sub>2</sub> Single Crystals Ion Implanted with 5 Kev Hydrogen. *J. Phys. D: Appl. Phys.* **2016**, *49* (10), 105108.
- (37) Susanne Siebentritt, U. R. *Wide-Gap Chalcopyrites*, 1st ed.; Springer-Verlag Berlin Heidelberg: 2006; p XIV, 260.
- (38) Rey, G.; Larramona, G.; Bourdais, S.; Choné, C.; Delatouche, B.; Jacob, A.; Dennler, G.; Siebentritt, S. On the Origin of Band-tails in Kesterite. *Sol. Energy Mater. Sol. Cells* **2018**, *179*, 142–151.
- (39) Kim, J.; Lee, S.-H.; Lee, J. H.; Hong, K.-H. The Role of Intrinsic Defects in Methylammonium Lead Iodide Perovskite. *J. Phys. Chem. Lett.* **2014**, *5* (8), 1312–1317.
- (40) Song, Z.; Wang, C.; Phillips, A. B.; Grice, C. R.; Zhao, D.; Yu, Y.; Chen, C.; Li, C.; Yin, X.; Ellingson, R. J.; et al. Probing the Origins of Photodegradation in Organic–inorganic Metal Halide Perovskites with Time-resolved Mass Spectrometry. *Sustainable Energy & Fuels* **2018**, *2* (11), 2460–2467.
- (41) Juarez-Perez, E. J.; Ono, L. K.; Maeda, M.; Jiang, Y.; Hawash, Z.; Qi, Y. Photodecomposition and Thermal Decomposition in Methylammonium Halide Lead Perovskites and Inferred Design Principles to Increase Photovoltaic Device Stability. *J. Mater. Chem. A* **2018**, *6* (20), 9604–9612.
- (42) Krustok, J.; Collan, H.; Yakushev, M.; Hjelt, K. The Role of Spatial Potential Fluctuations in the Shape of the PL Bands of Multinary Semiconductor Compounds. *Phys. Scr.* **1999**, *T79*, 179–182.
- (43) Varshni, Y. P. Temperature Dependence of the Energy Gap in Semiconductors. *Physica* **1967**, *34* (1), 149–154.
- (44) Francisco-López, A.; Charles, B.; Weber, O. J.; Alonso, M. I.; Garriga, M.; Campoy-Quiles, M.; Weller, M. T.; Goñi, A. R. Equal Footing of Thermal Expansion and Electron–phonon Interaction in

the Temperature Dependence of Lead Halide Perovskite Band Gaps. *J. Phys. Chem. Lett.* **2019**, *10* (11), 2971–2977.

(45) Saidi, W. A.; Poncé, S.; Monserrat, B. Temperature Dependence of the Energy Levels of Methylammonium Lead Iodide Perovskite from First-Principles. *J. Phys. Chem. Lett.* **2016**, *7* (24), 5247–5252.

(46) Hempel, H.; Dennler, G.; S, M.; x00Fc; ller; Larramona, G.; Eichberger, R.; Unold, T. Charge Carrier Dynamics in  $\text{Cu}_2\text{ZnSn}(\text{S}/\text{Se})_4$  Thin Film Solar Cells Measured by Time Resolved Terahertz and Microwave Spectroscopy, *2016 41st International Conference on Infrared, Millimeter, and Terahertz waves (IRMMW-THz)*, 25–30 Sept.; International Society of Infrared, Millimeter, and Terahertz Waves: 2016; pp 1–2.

(47) Wang, Y.; Long, R. Anomalous Temperature-dependent Charge Recombination in  $\text{CH}_3\text{NH}_3\text{PbI}_3$  Perovskite: Key Roles of Charge Localization and Thermal Effect. *ACS Appl. Mater. Interfaces* **2019**, *11* (35), 32069–32075.

(48) Liu, N.; Yam, C. First-principles Study of Intrinsic Defects in Formamidinium Lead Triiodide Perovskite Solar Cell Absorbers. *Phys. Chem. Chem. Phys.* **2018**, *20* (10), 6800–6804.

(49) Ma, F.; Li, J.; Li, W.; Lin, N.; Wang, L.; Qiao, J. Stable A/ $\Delta$  Phase Junction of Formamidinium Lead Iodide Perovskites for Enhanced Near-infrared Emission. *Chemical Science* **2017**, *8* (1), 800–805.

(50) Fu, M.; Tamarat, P.; Trebbia, J.-B.; Bodnarchuk, M. I.; Kovalenko, M. V.; Even, J.; Lounis, B. Unraveling Exciton–phonon Coupling in Individual  $\text{FAPbI}_3$  Nanocrystals Emitting Near-infrared Single Photons. *Nat. Commun.* **2018**, *9*, 3318.

(51) Thouin, F.; Valverde-Chávez, D. A.; Quarti, C.; Cortecchia, D.; Bargigia, I.; Beljonne, D.; Petrozza, A.; Silva, C.; Srimath Kandada, A. R. Phonon Coherences Reveal the Polaronic Character of Excitons in Two-dimensional Lead Halide Perovskites. *Nat. Mater.* **2019**, *18* (4), 349–356.

(52) Stoumpos, C. C.; Malliakas, C. D.; Kanatzidis, M. G. Semiconducting Tin and Lead Iodide Perovskites with Organic Cations: Phase Transitions, High Mobilities, and Near-Infrared Photoluminescent Properties. *Inorg. Chem.* **2013**, *52* (15), 9019–9038.

(53) Fang, H.-H.; Wang, F.; Adjokatse, S.; Zhao, N.; Even, J.; Antonietta Loi, M. Photoexcitation Dynamics in Solution-processed Formamidinium Lead Iodide Perovskite Thin Films For Solar Cell Applications. *Light: Sci. Appl.* **2016**, *5*, e16056.

(54) Ke, W.; Xiao, C.; Wang, C.; Saparov, B.; Duan, H.-S.; Zhao, D.; Xiao, Z.; Schulz, P.; Harvey, S. P.; Liao, W.; et al. Employing Lead Thiocyanate Additive to Reduce the Hysteresis and Boost the Fill Factor of Planar Perovskite Solar Cells. *Adv. Mater.* **2016**, *28*, 5214–5221.